Supplementary Information for:

Physical passivation of grain-boundaries and defects in perovskite solar cells by an isolating thin polymer

Efrain Ochoa-Martinez,[*,†] Mario Ochoa,[‡] Roberto D. Ortuso,[†] Parnian Ferdowsi,[†] Romain Carron,[‡] Ayodhya N. Tiwari,[‡] Ullrich Steiner,[†] and Michael Saliba[*,¶,§]

†Adolphe Merkle Institute, Chemin des Verdiers 4, CH-1700 Fribourg, Switzerland

‡Laboratory for Thin Films and Photovoltaics, Empa-Swiss Federal Laboratories for Materials Science and Technology, Ueberlandstrasse 129, CH-8600 Duebendorf, Switzerland

¶Institute for Photovoltaics (ipv), Pfaffenwaldring 47, 70569 Stuttgart, Germany

§Helmholtz Young Investigator Group FRONTRUNNER, IEK5 Photovoltaics, Forschungszentrum Jülich, 52425 Jülich, Germany

E-mail: efrain.ochoamartinez@unifr.ch; michael.saliba@ipv.uni-stuttgart.de

Phone: +41 26 300 8960; +49 (0)711 685-67140

Materials & Methods

Device fabrication

The organic solvents, DMF, DMSO and chlorobenzene were reagent-grade from Sigma Aldrich. The organic iodide and bromide salts were from Greatcell Solar Materials. The inorganic lead precursors (PbI_2 and $PbBr_2$) were from TCI, CsI was from Gute Chemie. The FTO substrates were TEC7 from Sigma Aldrich; prior to the device fabrication FTO was etched from one of the sides of the samples with Zn and HCl (2M) followed by rinsing in deionised (DI) water. The samples were then sonicated in a 2% (V:V) solution of Hellmanex III and DI water, followed by rinsing in water, sonication in ethanol and sonication in isopropyl alcohol for 15 minutes each, before drying in a nitrogen stream and plasma cleaning in an oxygen atmosphere for ten minutes. The electron transport layer and the meso porous layer were both composed of TiO_2; the first is a compact anatase layer produced by spray pyrolysis of a 6% solution (V:V) of titanium diisopropoxide bis(acetylacetonate) in ethanol. The spraying took place at 450 °C using approximately 0.05 ml/cm^2 of solution with oxygen as carrier gas. The mesoporous anatase layer was made with titania paste-30 NRD diluted at 100 mg/ml in ethanol and spin coated at 4000 rpm followed by an annealing at 450 °C in an air atmosphere. After cooling down the substrates were transferred to the glovebox.

For the preparation of the triple cation perovskite solution with composition $Cs_{0.05}(FA_{0.9}MA_{0.1})_{0.95}Pb(I_{0.9}Br_{0.1})_3$, 1.5M solutions of PbI_2 and $PbBr_2$ using a 4:1 (V:V) solution in DMF and DMSO were first prepared. The FAI and MAI salts were then weighted and mixed with the respective inorganic solutions in a stoichiometric proportion to result in 1.22M solutions of $FAPbI_3$ (with 9% excess of PbI_2 to improve crystallisation) and $MAPbBr_3$. These two solutions were mixed in a 90:10 (V:V) ratio. Finally, a 5% (V:V) of 1.5M CsI in DMSO was added. The antisolvent devices were produced in the nitrogen-filled glovebox by spin coating 40 µl of the perovskite solution at 3000 rpm during 30 s.; After spinning for 20 s, 100 µl of chlorobenzene were dropped on the spinning substrate. The spin-cast

layers were annealed at 100 °C for 45 min. The FIRA devices use the same substrates and similar perovskite solutions, with an adapted solvent ratio, 3:1 (V:V, DMF:DMSO). The solution deposition took place in a nitrogen-filled glovebox by spin-coating at 4000 rpm, without antisolvent deposition. After spin coating, the samples were transferred to the FIRA oven and irradiated with 9 kW infrared light for 1.2 s. For PMMA deposition (analytical standard for GPC, MW~10,000), 50 µl of 0.1 mg/ml solution in chlorobenzene were deposited by spin-coating at 4000 rpm for 20 s. All the devices were finished by depositing the hole transport material consisting of 50 µl of a 70 mM solution of Spiro-OmeTAD in chlorobenzene doped with 1 µl of 1.8 M of Lithium salt (LiTFSI) in acetonitrile, and 1.8 µl of 4-tert-butylpyridine, by spin coating for 20 s at 4000 rpm. The back electrode was deposited by evaporating 120 nm of silver. The final device stack was glass/FTO/c-TiO_2/mesoporous-TiO_2/perovskite/(PMMA)/Spiro/Ag.

Time resolved photoluminescence

The TRPL mapping system is based on PicoQuant components. It uses a FluoTime 300 unit and a microscope system (MicroTime 100). For excitation, a 639 nm laser with a ~100 ps pulse width and a frequency of 300 kHz was used. The beam diameter was roughly 130 µm (13.5% metric), measured with a NanoScan2 beam profiler. The excitation photon density was $\sim 6 \times 10^{11}$ photons/cm^2/pulse. The emitted light was collected with an Olympus long-range 20× objective (LCPLN20XIR) with numerical aperture of 0.45 and then guided into a 50 µm detection fiber acting as a pinhole, which was coupled to the FluoTime unit including the input optics to focus the light onto to the monochromator and the photomultiplier detector (PMA 192). A Time-Harp 260 Nano TCPSC card in long-range mode was used for photon counting. A wide range scanner stage from Physik Instrumente (M687.7) was used for mapping. The dwell time was set to 5 ms/decay with a step size of 0.5 µm/pixel. The resulting image size was 400×400 pixels. The system has a global illumination – local detection configuration (widefield) with an optical resolution ~2 µm. The signal decays

were not fully mono-exponential at each pixel. Fitting a two-exponential decay had a minor impact on the spatial distributions and single exponential fits were therefore used.

Atomic force microscopy

AFM images were taken by a Park NX10 instrument (Park Systems Corp., Suwon, Korea), equipped with the Smart Scan software version 1.0 RTM 12d. All measurements were performed in an acoustic enclosure (JPK Instruments AG, Berlin, Germany) equipped with antivibration table (e-Stable mini, Kurashicki Kako Co., LTD, Okayama, Japan). TAP300AL-G (Budget Sensors, Sofia, Bulgaria) tips with declared tip radii of less than 10 nm were used for imaging . No tip deconvolution was applied to the acquired images, inducing a systematic error in the xy-plane size definition that is dependent on the exact tip shape and size. Tip spring constants and instrument sensitivity were measured after each tip was mounted, using of the Sader method[1] and tip displacement method, respectively.[2] For all tips, tip spring constants were within the range declared by the manufacturer. All images were taken in tapping mode. Imaging parameters were kept constant with a free oscillation amplitude of 700 ± 30 nm, a set point of 360 ± 40 nm, an integral gain of 1 ± 0.5 A.U., a proportional gain of 1 ± 0.5 A.U., and a scanning rate of 0.4 ± 0.05 Hz. The scan range was 1024×1024 pixels, independent of the imaging scale. For both the antisolvent and FIRA samples, reference samples and those with PMMA treatment were measured on the same day using fresh samples, with the same tip and same AFM calibration, avoiding artefacts that could arise from altered atmospheric or experimental conditions.

The raw AFM data was analysed using the Gwyddion software (Version 2.54, GNU licencing). All data were treated in the same way to maximize comparison between datasets. The height images were levelled by "mean plane subtraction" to remove sample tilt, followed by a 1st order polynomial baseline removal of each fast scan line. To remove bowing artefacts from the height channel, a 2nd order polynomial baseline removal was first applied along slow scan direction, followed by a subtraction along the fast scan direction. Forward and

backward height signals were then averaged, giving the resulting height images. The phase channel was treated by by "mean plane subtraction" to remove the sample tilt, followed by 1st order polynomial baseline removal of each fast scan line. No further corrections were applied. The look up table (LUT) was adjusted to increase contrast of image features. The phase data were exported as text files, imported in MATLAB for histogram analysis. Fityk (Version 1.3.1, GNU licencing) was used for the deconvolution of the histogram data.[3] Gaussian fits were used, the number of deconvolutions was varied until RMS errors of the sum of fits and original histogram signal was within the same range. Colour coded images were created by MATLAB thresholded binary images, in which the white pixels were then coloured using the GIMP software (Version 2.10.12, GNU licencing).

Other characterizations

XRD analysis was performed in annealed films with the layer sequence glass/FTO/c-TiO$_2$/mesoporous-TiO$_2$/perovskite using a Rigaku Ultima IV x-ray diffractometer, equipped with a Cu x-ray source and in the Bragg-Brentano configuration. Electron microscopy was carried out using a ThermoFischer Scios 2 SEM-FIB system. Optical microscopy was carried out using a ZEISS Axio Scope.A1 microscope with a 20x air objective, NA 0.6. Optical micrographs were captured with a CCD camera (GS3-U3-28S5C-C, Point Grey/ FLIR Integrated Imaging Solutions Inc., Richmond, Canada). The current-voltage characteristics of the finished devices were acquired by illumination with an ABET Technologies Sun 3000 Solar simulator through a shadow mask defining a pixel of 0.1 cm^2. The simulator intensity was calibrated after a reference cell with KG5 filter glass. The ellipsometry measurements were performed using an Alpha-SE spectroscopic ellipsometer from Woollam. Long-term stability measurements were carried out in nitrogen atmosphere flushed at 0.5 L/min, the temperature was constantly controlled at 20 C, illumination was provided by RGB LEDs that matched to the solar spectrum and intensity matched using current matching of a Si reference diode.

Photovoltaic cell diode model and R_{SH}

The equations below are based on a diode model, which describe the $I - V$ relation of an illuminated PV cell including series (R_S) and shunt (R_{SH})resistances, where I_{ph} is the photogenerated current, I_0 the diode saturation current, n the ideality factor, k the Boltzmann constant and T the temperature.

$$I = I_{ph} - I_0 e^{\frac{q(V+IR_S)}{nkT}} - \frac{V + IR_S}{R_{SH}} \tag{S1}$$

$$V_{oc} = \frac{nkT}{q} \ln \left[\frac{I_{ph}}{I_0} \left(1 - \frac{V_{oc}}{I_{ph}R_{SH}} \right) \right] \tag{S2}$$

The equations show that decreasing R_S and increasing R_{SH} maximises V_{oc}. Equation S1 allows the measurement of R_{SH} as the negative value of the derivative dV/dI at the point of short circuit $(V = 0)$.

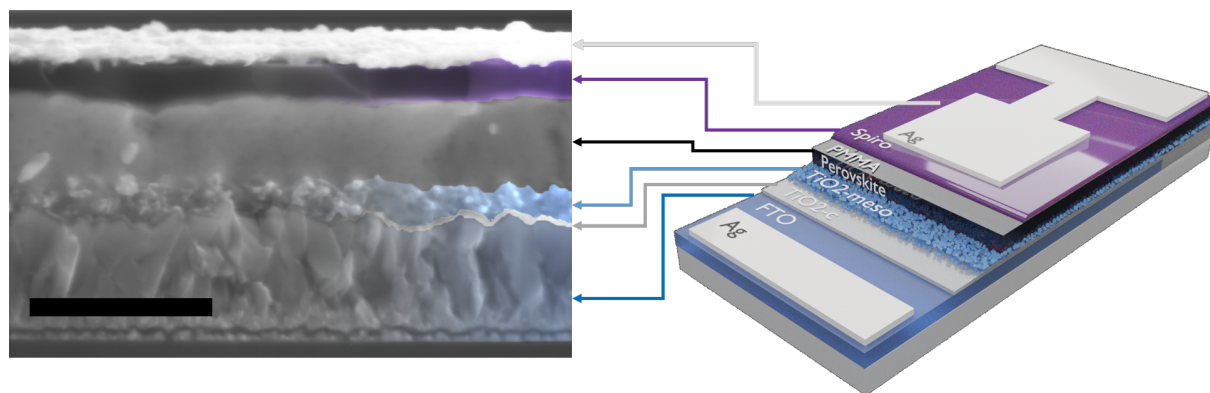# Supporting figures and table

Figure S 1: Cross section showing the layer stack (left) and schematic device structure (right) of an antisolvent PSC. FIRA devices share the same layer structure. Scale bar: 1 µm.
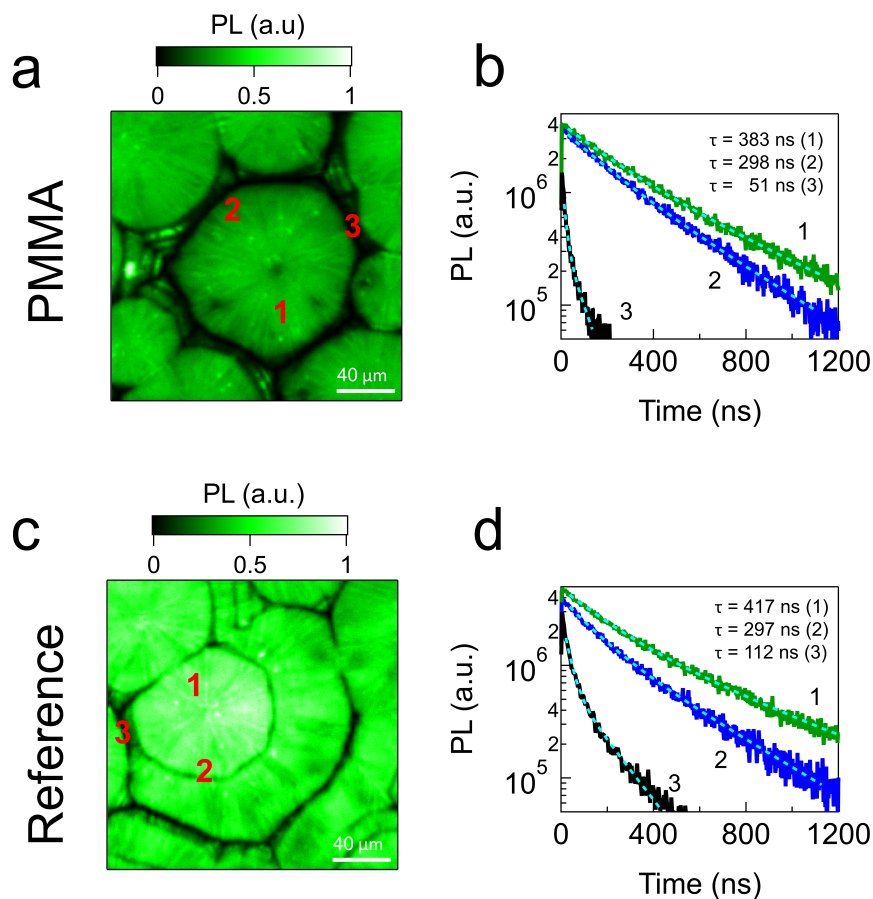
Figure S 2: Normalized time-integrated PL maps for FIRA samples after PMMA deposition (a) and the reference sample (c). PL transients averaged over 100 pixels are also shown in (b) and (d) for PMMA and reference sample, respectively. Three different transients per sample are shown corresponding to regions within the main domain (1) close to the border of the domain (2) and in a domain boundary (3). The lifetime values depicted in the legend of (b) and (d) correspond to average lifetime from a dual-exponential equation.

A possible explanation for the faster lifetimes at the domain boundaries upon PMMA deposition is the reduction of both, interface recombination and charge accumulation. PMMA can contribute to passivation, lowering interface recombination, which in turn reduces the interface charge favouring electron extraction from the absorber to the ETL. Such extracted electrons do not contribute to the PL signal, thus lowering the carrier lifetime.
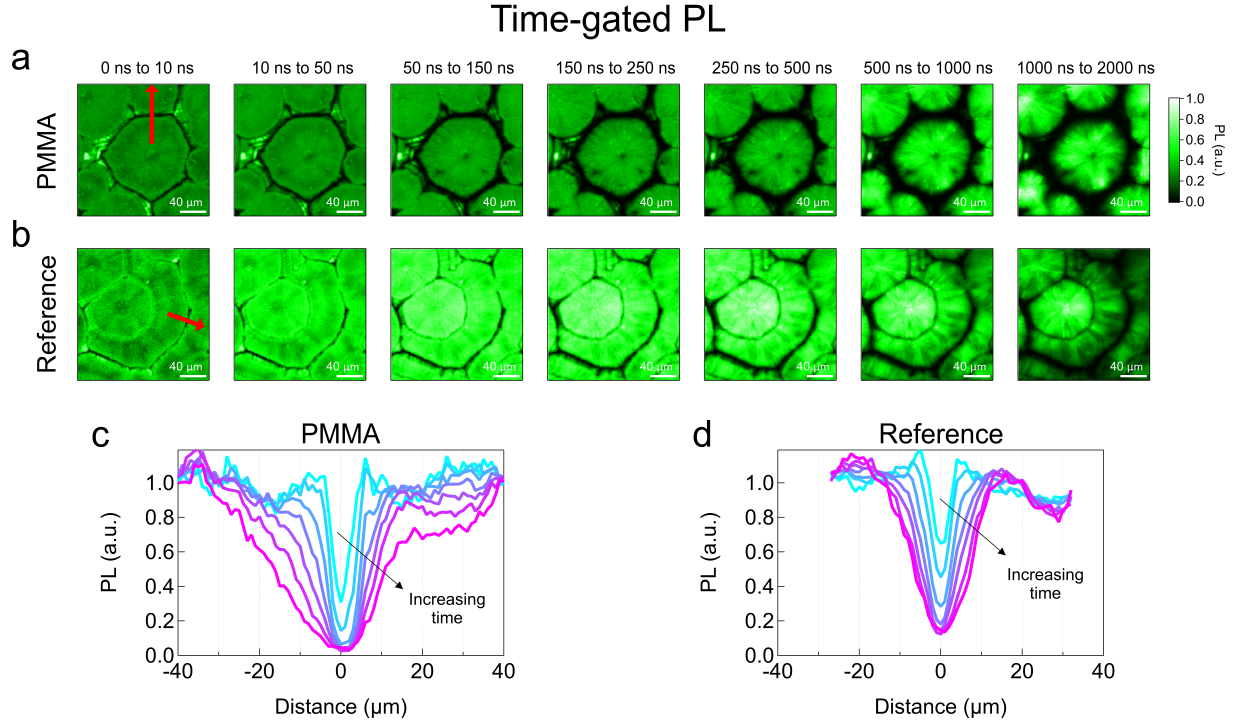
8

Time-gated PL

Figure S 3: Normalized time-gated PL maps of FIRA samples for a) PMMA a) and b) reference. Each PL map corresponds to the integrated PL for several time gates shown in the top of PMMA maps. PL line profiles of c) PMMA and d) reference for each time-gated PL map are also depicted. The red arrows in the first time gate map (0 ns to 10 ns) of a) and b) indicate the location where the line profiles were taken for all time gates.

For PMMA and reference, the domain boundary width at the initial times is $\sim 10\,\mu$m, in agreement with the lower material height measured by AFM (Figure 1d), and suggests that both domain boundaries are physically similar. Electronically, the behaviour is different for each sample. By comparing the PL maps at initial and later times, we find that PMMA influences the PL signal in a wider region of $\sim 35\,\mu$m around the domain boundary (distance from zero in Figure S3c), as compared to $\sim 15\,\mu$m for the reference.
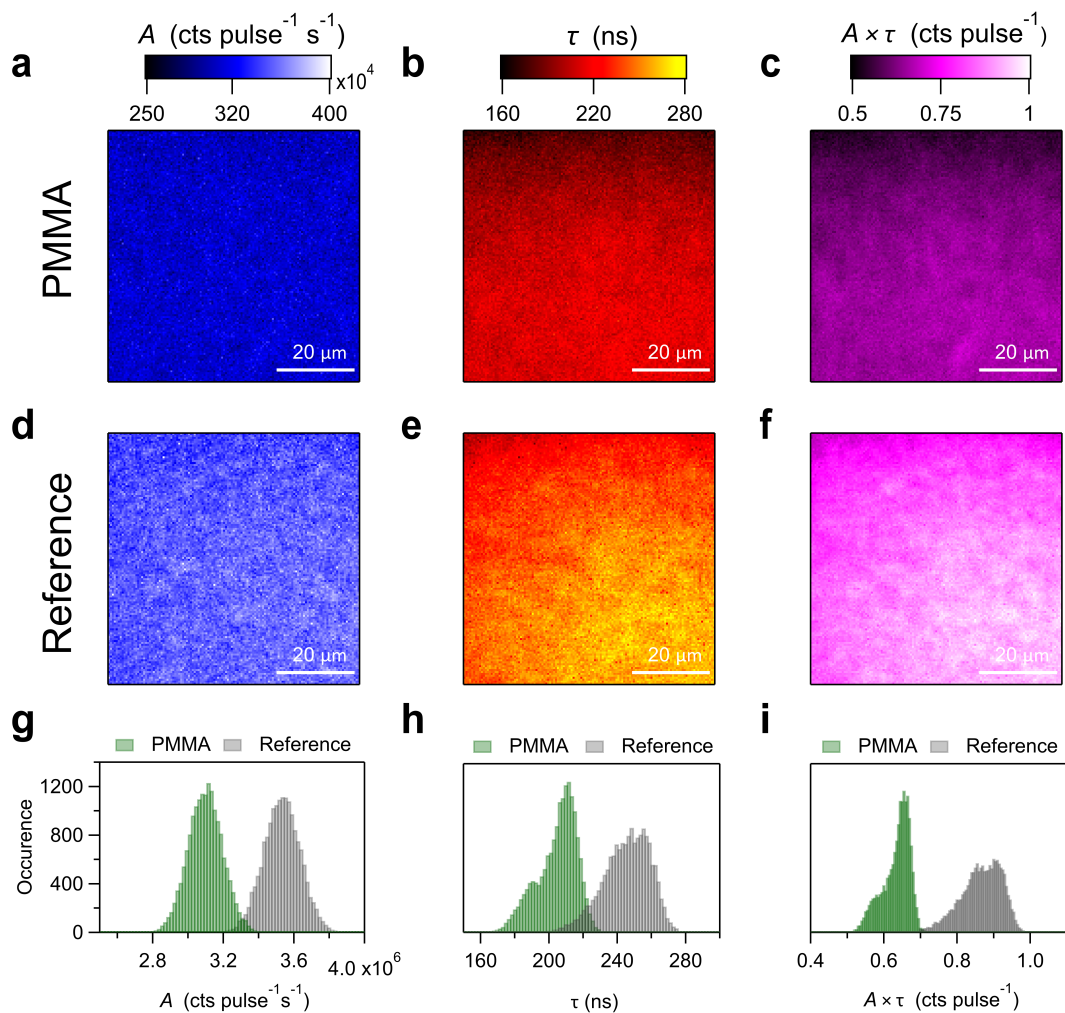
Figure S 4: Spatially resolved TRPL maps of antisolvent triple cation perovskite films showing amplitude (A), lifetime (τ), and $A \times \tau$ for films with (a-c) and without (d-f) PMMA treatment. Below, histograms of amplitude (g), lifetime (h), and lifetime $\times$ amplitude (i).
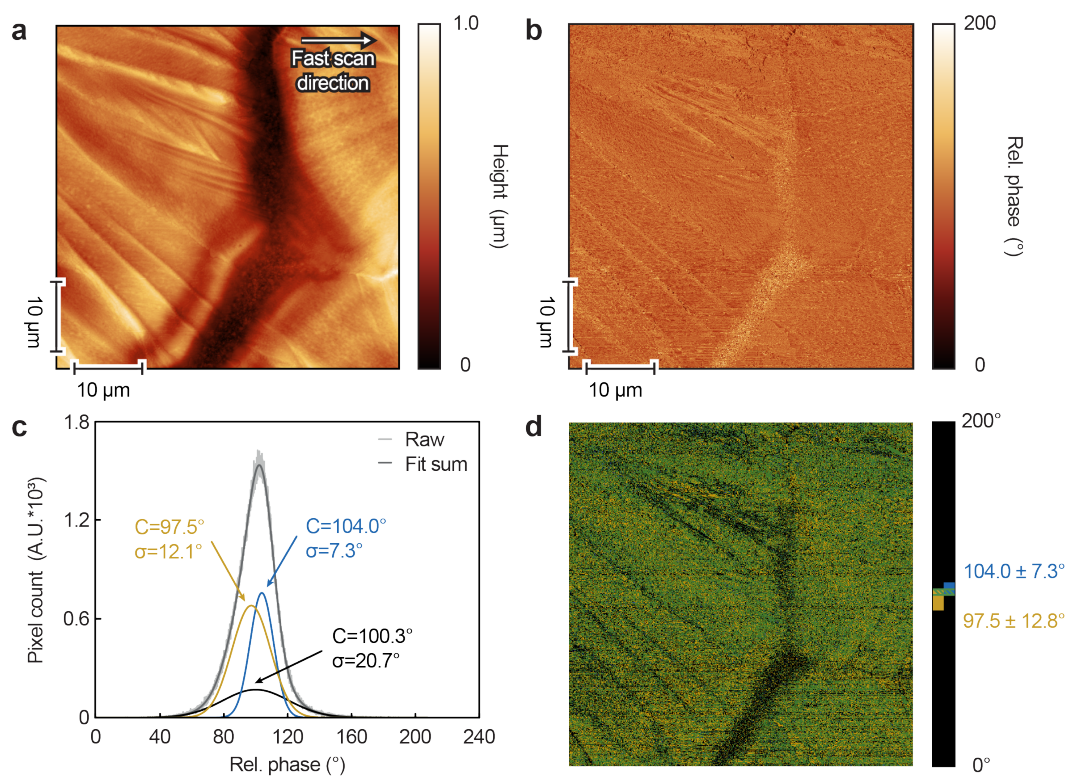
Figure S 5: AFM scan showing a domain boundary of a treated flash annealed triple cation perovskite film, in the absence of PMMA treatment. a) Height image (topography), b) phase channel, c) phase histogram and deconvolution analysis. d) Segmented colour coded image of phase channel.
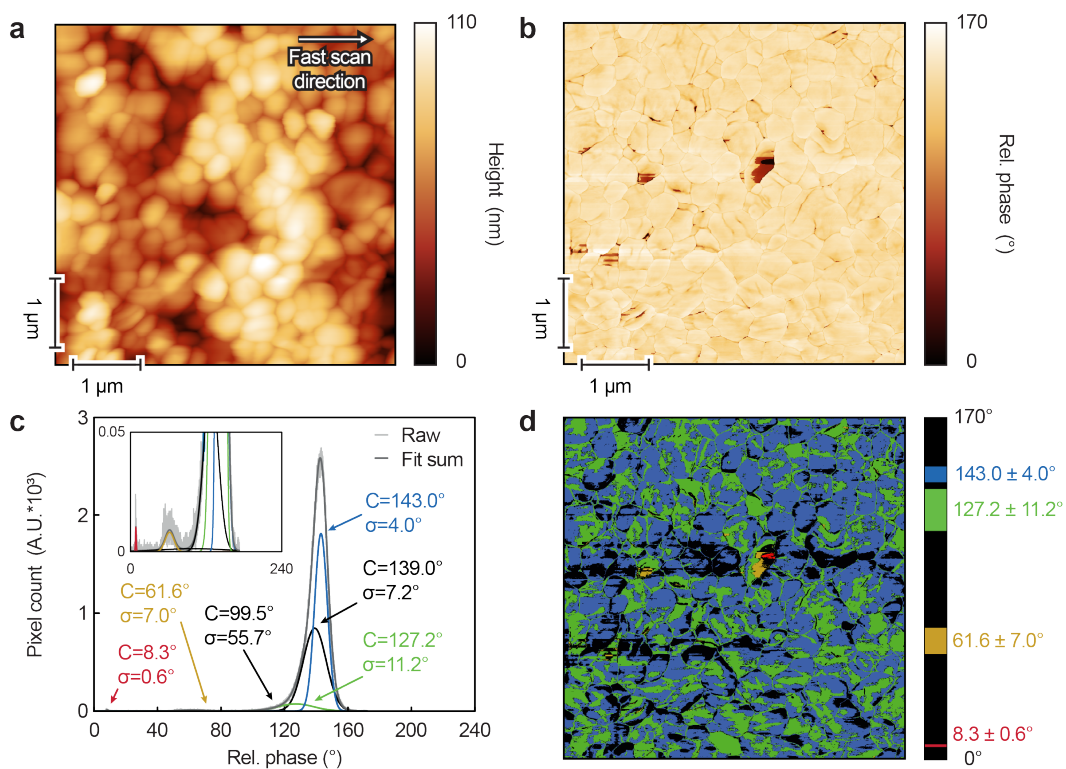
Figure S 6: AFM scan of a triple cation perovskite film made by the antisolvent method, in the absence of PMMA treatment. a) Height image (topography), b) phase channel, c) phase histogram and deconvolution analysis, and d) colour coded segmented image.
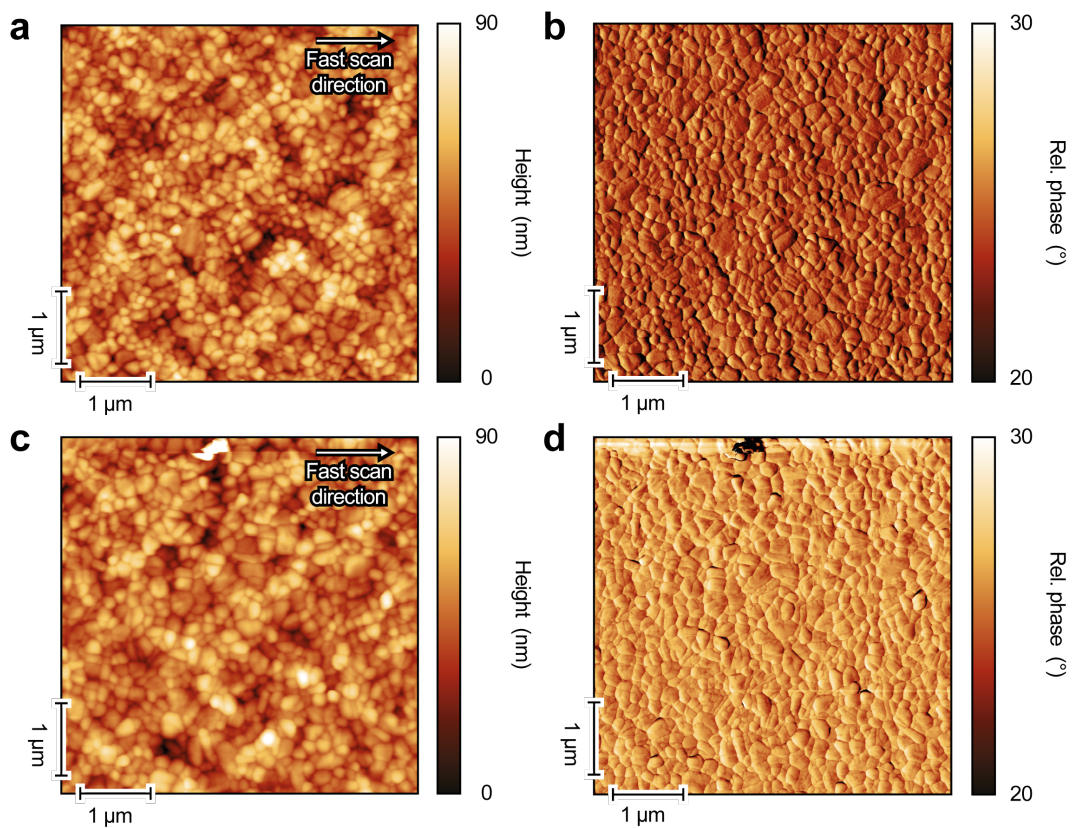
Figure S 7: AFM scans of two sections of the same triple cation perovskite film made by the antisolvent method, as deposited (top) and after chlorobenzene wash (bottom). a) Height image (topography, mean value 46.1 ± 8.7 nm) and b) phase channel of pristine sample $(24.0 \pm 0.2°)$. c) Height image (topography, mean value 45.4 ± 9.3 nm) and d) phase channel of solvent washed sample $(25.8 \pm 1.2°)$.
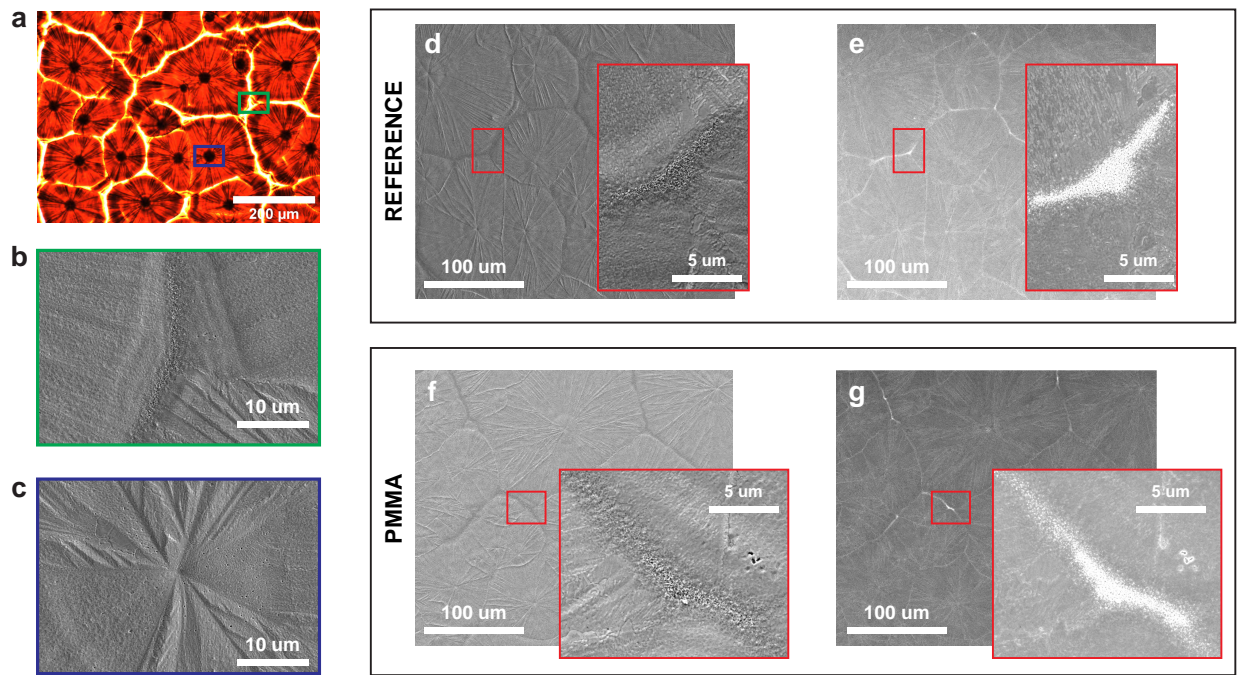
Figure S 8: Detailed microscopy analysis of FIRA annealed perovskite layers by a) transmission optical microscopy image. SEM details of b) a domain boundary and a c) domain centre. d-f) Comparisons of secondary (d and f) and backscattered (e and g) SEM images of reference and PMMA treated FIRA perovskite layers. The insets show uncovered inter-domain regions.
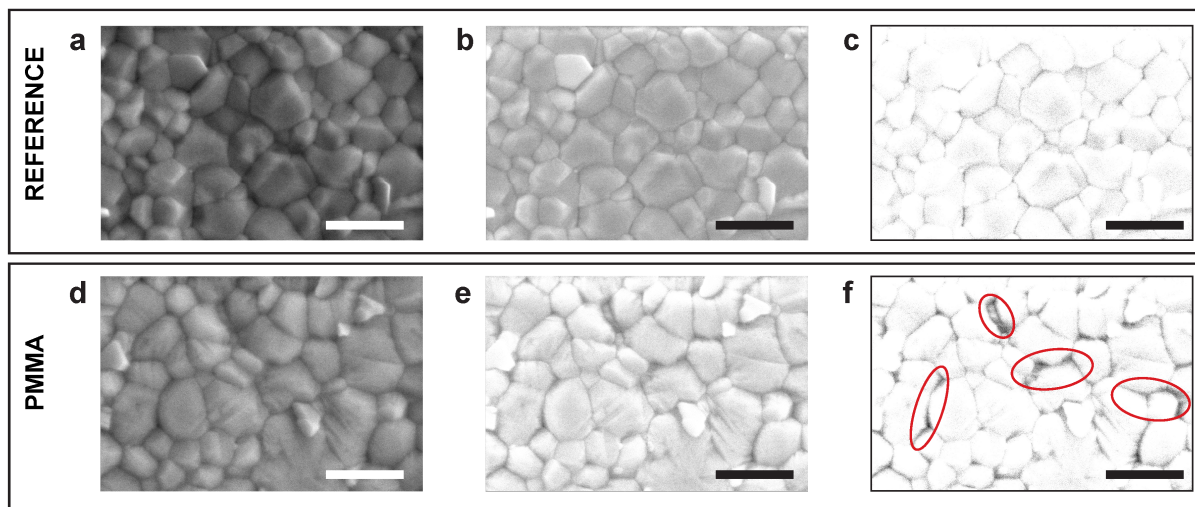
Figure S 9: Secondary (a, d) and backscattered (b, e) SEM images of reference and PMMA treated perovskite layers made by antisolvent method. c,f show backscattered SEM images in which the contrast was enhanced. Scale bar: 500 nm.

In standard SEM, secondary electrons are used to image the topography of a sample. Backscattered electrons allow mapping lateral differences in composition, with lighter colours denoting heavier elements. This method allows to infer that the FTO substrate is visible at some inter-domain borders of FIRA samples in Figure S8, where the bright signal probably arises from tin. After the PMMA treatment, the presence of these uncovered regions is significantly reduced, probably due to PMMA partially covering these gaps. For antisolvent devices the behaviour is similar, when analysed in BSE mode (Figure S9b,e) i.e. grain boundaries have a lower signal (appear darker) for samples treated with PMMA. A contrast change allows an even better identification of these areas (Figure S9c,f).
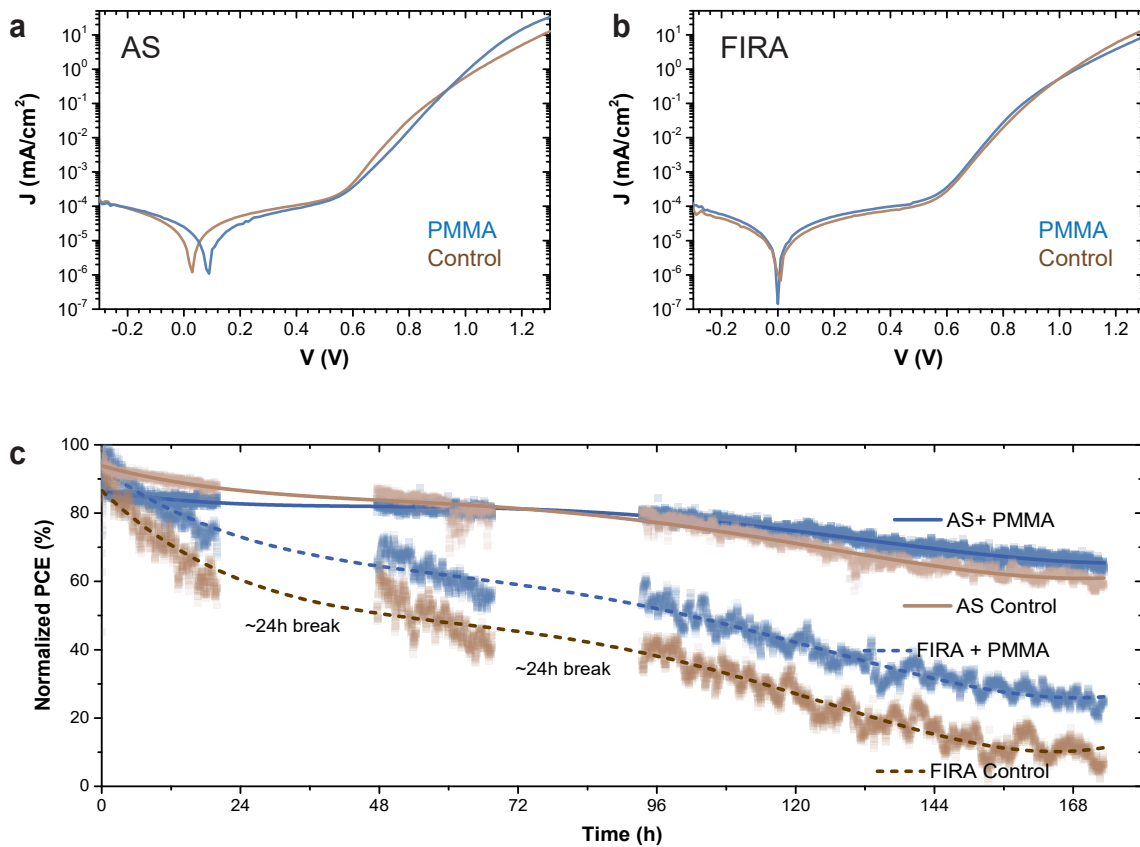
Figure S 10: Dark J-V measurements of a) AS, and b) FIRA samples. c) Maximum power point tracking of unecampsulated devices under continuous operation at 20 °C in N_2 atmosphere at an equivalent irradiance of 1 sun.
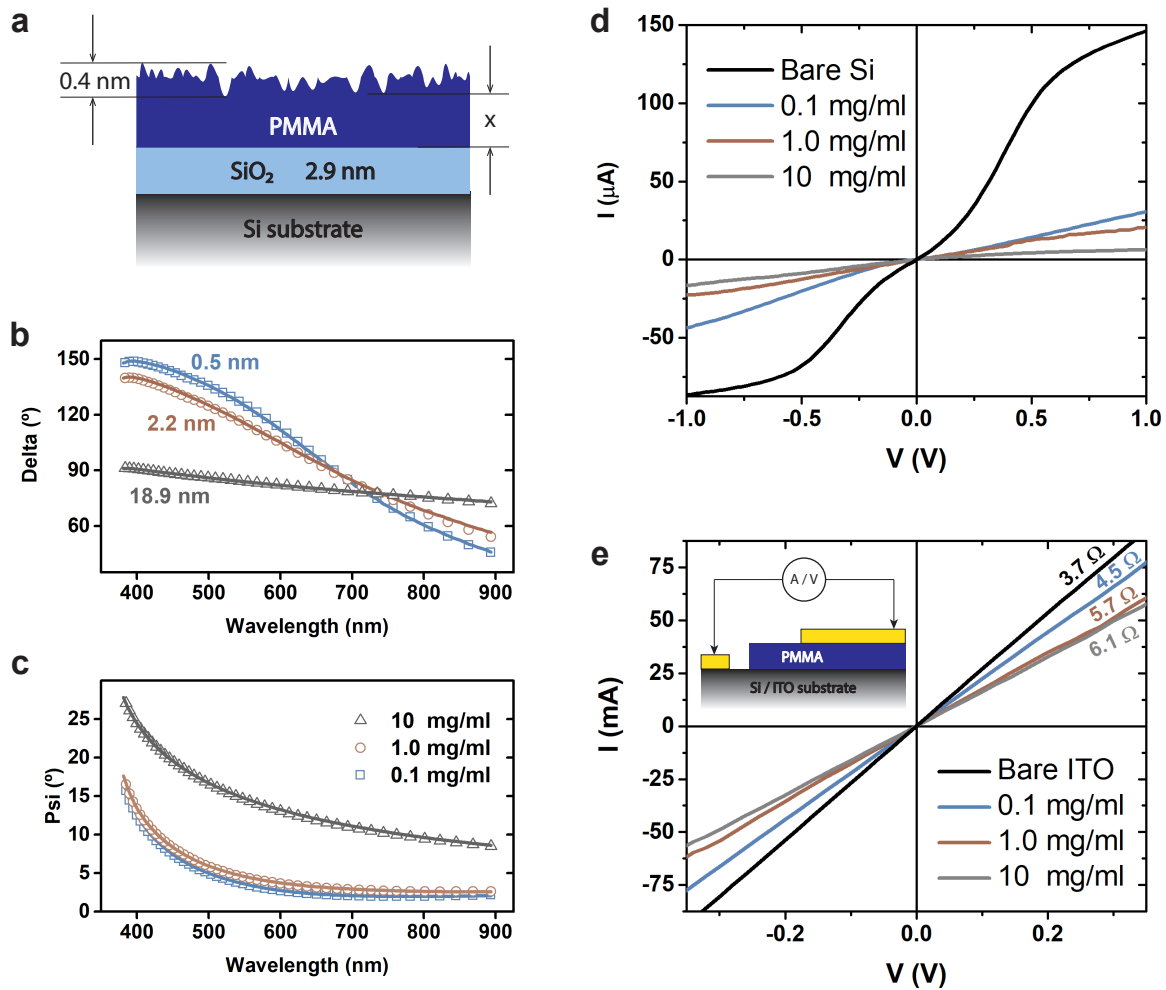
Figure S 11: Left: a) Layer structure used in the ellipsometry analysis (not to scale), and b), c) ellipsometric angles measured at an incidence angle of 75° (open symbols) and fitting results (full lines) for PMMA layers deposited on silicon wafers. Right: I-V measurements across PMMA layers prepared with different solution concentrations on d) polished Si and e) ITO substrates. The inset in e) shows a schematic of the experimental configuration.

The effective medium model used to analyse the ellipsometry data is shown in Figure S11a, which includes a surface roughness of the deposited PMMA film measured by AFM of ≈ 0.4 nm for all films. Note that this model study of laterally continuous PMMA films does not reflect the AFM study of Figure 3 showing that PMMA deposition onto perovskite layers does not result in uniform conformal films, but in an accumulation of PMMA in cavities and other topographic depressions.
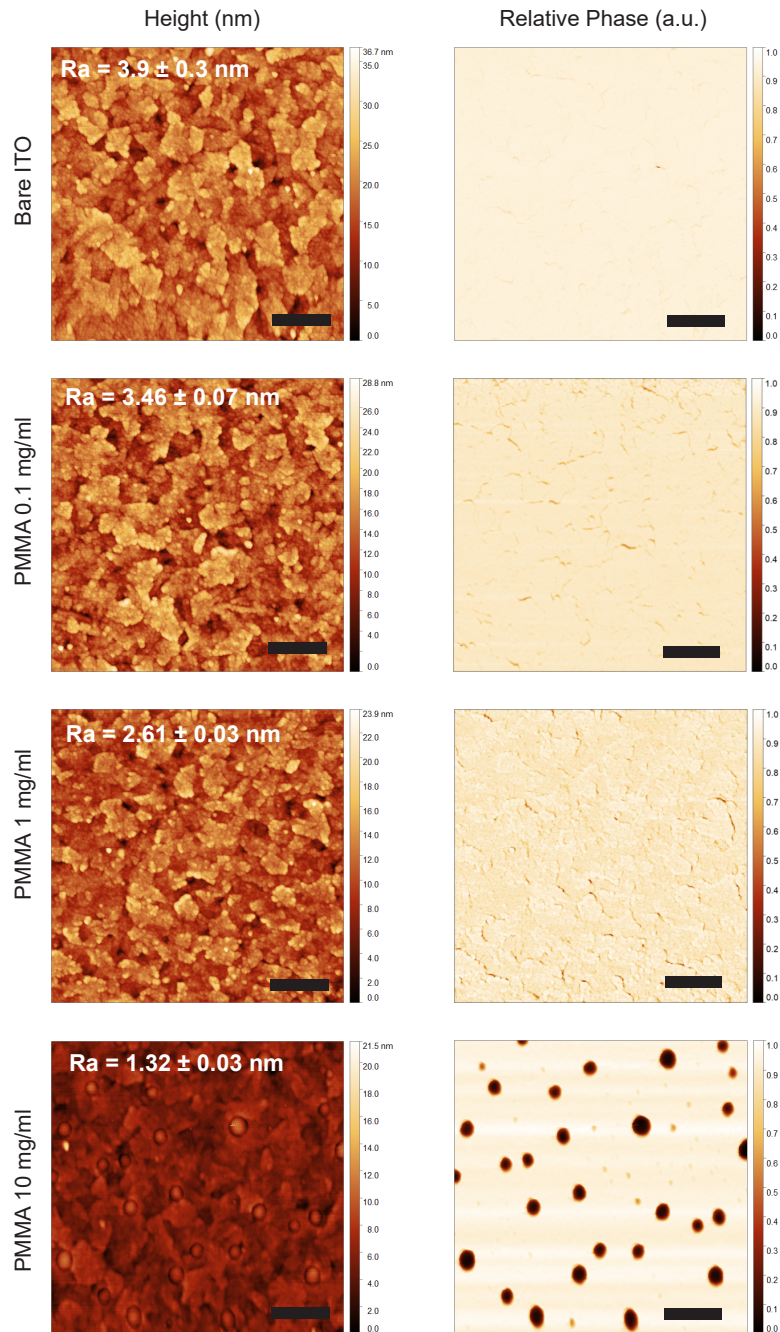
17

Figure S 12: AFM scans of bare ITO (top) and PMMA treated ITO samples, showing height (left) and relative phase (right). Phase scans have been normalized to enhance the contrast between PMMA and ITO dividing the phase values by 61, 44.5, 22.2 and 69 for the phase scans of the bare ITO, 0.1, 1.0 and 10 mg/ml respectively. Scale bar: 1 µm.

Table S 1: Control and treated champion cell parameters according to device structure and perovskite composition for bibliographic references using polymer interlayers, IL stands for the interlayer under study.[4–9]

Cell structure & architecture	Perovskite composition	Interlayer (IL) composition	*Interlayer concentration* (mg/ml)	Control Cell J_{sc} (mA/cm²) V_{oc} (V) FF (%) PCE (%)	Treated Cell J_{sc} (mA/cm²) V_{oc} (V) FF (%) PCE (%)	Reference
ITO/PTAA/PVK/**IL**/C60/BCP/Au (*p-i-n* planar)	MAPbI$_3$	PS	0.2 – 20 Best at 10 mg/ml	21.1 1.07 74.9 16.9	22.9 1.10 80.6 20.3	Wang, Q., et al, 2016[4]
ITO/PEDOT:PSS/PVK/**IL**/Au (*p-i-n* planar)	MAPbI$_{3-x}$Cl$_x$	PCBM:PMMA	0.5 – 2 Best at 1 mg/ml	18.8 0.98 64.4 11.9	18.5 1.03 75 14.3	Bi, S., et al., 2017[5]
FTO/cTiO2/mTiO2/PVK/**IL**/Spiro/Au (*n-i-p* meso)	MAPbI$_3$	PMMA	5 – 30 Best at 10 mg/ml	21.5 1.01 67 14.6	22.0 1.03 72 16.4	Wang, F., et al., 2017[6]
FTO/cTiO2/mTiO2/**IL1**/PVK/**IL2**/Spiro/Au* (*n-i-p* meso)	CsRbFAMAPbIBr	PMMA (*for IL2*)	1 mg/ml*	22.8 1.17 76.2 20.3	22.6 1.21 76.1 20.9	Peng, J., et al., 2018[7]
ITO/TiO$_2$/PVK/**IL**/Spiro/Au (*n-i-p* planar)	CsFAMAPb(IBr)$_3$	PMMA	2.5 – 10 Best at 5 mg/ml	22.9 1.15 72.1 19.0	22.8 1.18 76.5 20.6	Liu, P., et al., 2020[8]
ITO/SnO$_2$/**IL**/PVK/Spiro/Ag† (*n-i-p* planar)	Cs$_{0.15}$FA$_{0.85}$PbI$_3$	PMMA:C$_{60}$	1 mg/ml†	22.2 1.06 70.5 16.6	22.5 1.09 76.9 18.8	Chen, Y., et al., 2020[9]
FTO/cTiO2/mTiO2/PVK/**IL**/Spiro/Ag (*n-i-p* meso)	CsFAMAPb(IBr)$_3$	PMMA	0.1 mg/ml	22.1 1.09 80.2 19.4	22.3 1.09 83.6 20.4	This work

---

*Peng, J., et al. used a double interlayer architecture made by static spin coating deposition. The control device had one interlayer (**IL1**), without **IL2** (PMMA).

†Chen, Y., et al., used a double interlayer architecture with PMMA below the perovskite in a planar *n-i-p* device. The tabulated results correspond all to devices without the top PTABr treatment.

References

(1) Sader, J. E.; Chon, J. W. M.; Mulvaney, P. Calibration of rectangular atomic force microscope cantilevers. *Review of Scientific Instruments* **1999**, *70*, 3967–3969.

(2) Hutter, J. L.; Bechhoefer, J. Calibration of atomic-force microscope tips. *Review of Scientific Instruments* **1993**, *64*, 1868–1873.

(3) Wojdyr, M. Fityk: a general-purpose peak fitting program. *Journal of Applied Crystallography* **2010**, *43*, 1126–1128.

(4) Wang, Q.; Dong, Q.; Li, T.; Gruverman, A.; Huang, J. Thin Insulating Tunneling Contacts for Efficient and Water-Resistant Perovskite Solar Cells. *Advanced Materials* **2016**, *28*, 6734–6739.

(5) Bi, S.; Zhang, X.; Qin, L.; Wang, R.; Zhou, J.; Leng, X.; Qiu, X.; Zhang, Y.; Zhou, H.; Tang, Z. Incorporating an Inert Polymer into the Interlayer Passivates Surface Defects in Methylammonium Lead Halide Perovskite Solar Cells. *Chemistry – A European Journal* **2017**, *23*, 14650–14657.

(6) Wang, F.; Shimazaki, A.; Yang, F.; Kanahashi, K.; Matsuki, K.; Miyauchi, Y.; Takenobu, T.; Wakamiya, A.; Murata, Y.; Matsuda, K. Highly Efficient and Stable Perovskite Solar Cells by Interfacial Engineering Using Solution-Processed Polymer Layer. *The Journal of Physical Chemistry C* **2017**, *121*, 1562–1568.

(7) Peng, J. et al. A Universal Double-Side Passivation for High Open-Circuit Voltage in Perovskite Solar Cells: Role of Carbonyl Groups in Poly(methyl methacrylate). *Advanced Energy Materials* **2018**, *8*, 1801208.

(8) Liu, P.; Liu, Z.; Qin, C.; He, T.; Li, B.; Ma, L.; Shaheen, K.; Yang, J.; Yang, H.; Liu, H.; Liu, K.; Yuan, M. High-performance perovskite solar cells based on passivating interfacial and intergranular defects. *Solar Energy Materials and Solar Cells* **2020**, *212*, 110555.

(9) Chen, Y.; Shi, J.; Li, X.; Li, S.; Lv, X.; Sun, X.; Zheng, Y.-Z.; Tao, X. A universal strategy combining interface and grain boundary engineering for negligible hysteresis and high efficiency (21.41%) planar perovskite solar cells. *Journal of Materials Chemistry A* **2020**, *8*, 6349–6359.